Humidity dependent reversible transitions in gold nanoparticle superlattices

Casper Kunstmann-Olsen, Domagoj Belić, Dan F. Bradley, Marcin P. Grzelczak, and Mathias Brust*

University of Liverpool, Department of Chemistry,

Crown Street, Liverpool L69 7ZD, United Kingdom

E-mail: mbrust@liverpool.ac.uk

Abstract

The changes in interparticle spacing upon hydration and dehydration of drop-cast films of hydrophilic gold nanoparticles (GNP) have been measured *in-situ* with nanometer resolution using WetSTEM and ESEM. These subtle variations correlate well with the corresponding changes in the optical spectra and perceived color as well as changes in the electrical conductivity of the films. AC impedance analysis allows to differentiate between resistive and capacitive components and to evaluate how these depend on average particle spacing and the water content of the matrix, respectively. Thin films of this type are well known structures used for development of sensors and diagnostics.

Introduction

Thiolate-capped gold nanoparticles commonly referred to as monolayer protected clusters (MPCs), have been extensively studied over the past two decades.[1–4] One of their most promising "real life" applications is the use of superlattices of particles as active components

in artificial-nose-type sensing devices.[5,6] The first report on using MPCs in gas sensors was published by Wohltjen and Snow[7] in 1998 followed by a gradually growing body of similar work.[8–14] While ambient sensing generally focuses on the electrical conductivity of MPC superlattice films as the critical parameter, transitions in optical and structural properties also occur in these materials. Such phenomena have been extensively studied by Korgel and coworkers including temperature induced structural transitions.[15–17]

Perhaps the most exciting recent development in this field of research, has been the work by Haick *et al.* on lung cancer diagnostics based on analyzing patients' breath with an array of different MPC film sensors.[18–20] Since electrical conductance through MPC films occurs by electron hopping from particle to particle, changes in average interparticle spacing and in the composition of the matrix material greatly affect its value. While sensing is broadly based on these dependencies, the detailed specific responses to any particular environmental analyte are usually not fully understood, in part, because it is very difficult to obtain high-resolution data on the molecular scale interactions between the analyte and the sensing material. Not only the conductivity, but also the optical properties of gold nanoparticle films depend strongly on particle spacing and on the matrix refractive index.[21–23] In general, a slight broadening and red-shift of the plasmon band resulting in a change of perceived color from red to blue is observed as the particle spacing decreases.[24,25] This has been particularly well illustrated and quantitatively explained based on Mie theory, by Mulvaney *et al.* using families of Au@SiO_2 core-shell particles with a range of different shell thicknesses to control the spacings between the metallic cores.[22] Manipulating the optical properties in similar ways has been realized in a range of self-assembled plasmonic structures comprised of mixtures of various nanomaterials.[26–28]

In sensor devices, the changes in interparticle distance are often more subtle, and the corresponding changes in the optical properties are usually quite small. However, various methods have recently been developed to measure differential changes in absorbance for fixed wavelengths, creating multiplexed vapor sensors with high sensitivity.[29–31] Furthermore, there is

an entire field of science dedicated to the development of new optical biosensors[32] and assay formats based on color changes of gold nanoparticles upon aggregation.[33–40]

The electrical properties of ligand-stabilized GNP films, have been widely studied over the years.[7–14,18–20,41–43] The critical parameters are particle core size, interparticle spacing, and the dielectric constant of the matrix material. As expected, shorter ligands and larger particle core-size lead to materials with higher conductivity, whereas longer ligands and smaller core-sizes result in lower conductivity.[44] The dominant mechanism of electron transport through these materials is thermally activated electron-hopping.[41–43] The dielectric properties of the matrix mainly affect the capacitance between the particles and depend on the chemical identity of the ligand and the nature of the environmental molecules, for example, water.

Engineering the chemistry of the ligand is a versatile way of modulating the conducting properties of nanoparticle assemblies. Tuning key parameters such as particle-particle distance, electronic coupling between particles, and dielectric environment has been widely explored.[44–46] For example, Wessels et al.[10] showed that fully conjugated ligands (a benzene core with dithiocarbamate group) can increase conductance significantly relative to a non-conjugated ligand (cyclohexane with a thiol group) because of the lower charge-transfer energy barrier of the fully conjugated ligand. Stansfield and Thomas[47] revealed a substitution effect of the gold nanoparticles modified by an arylthiol ligand, in which electron-withdrawing substituents markedly increase conductivity.

While it is known that the relative humidity (RH) affects the sensitivity of GNP based VOC-sensors,[8,39,48] most investigations are concerned with hydrophobic analytes and water is considered an inconvenience.

We and others have recently documented the ability to image by environmental scanning electron microscope (ESEM) and wet scanning transmission EM (WetSTEM) fully hydrated thin films of hydrophilic gold nanoparticles and nanorods, respectively, at high enough resolution to study the ordering of individual particles with respect to each other.[49,50] De Jonge and colleagues have imaged the movement of GNP at a solid/liquid interfaces Scanning

Transmission Electron Microscopy (STEM) using a special liquid cell.[51]

Here we present a detailed study in which the macroscopic properties (color and conductivity) of hydrophilic gold nanoparticles under various conditions of hydration and dryness are correlated with the nanoscopic structure of the films as analyzed by ESEM and WetSTEM. This offers direct insight into the reversible structural changes occurring in MPC based materials during the sensing process.

Results and discussion

Structural response

Moderately polydisperse PEG-thiol-stabilized gold nanoparticles with a size distribution centered at 19 nm (see figure SI1 in SI) were drop cast from ethanolic dispersion onto carbon coated TEM sample grids and inspected by WetSTEM under various conditions of relative humidity (RH) from 0% to 100%. Figure 1 shows dark field (DF) WetSTEM images of the GNP assemblies at 100% and 0% RH. Note that the structural differences between the two extreme cases are subtle, but significant (see also animation ESIA1-3 in SI). While the fully hydrated samples appears as quite homogenous rafts of particles with uniform interparticle distances, in the completely dry sample, clusters of particles with reduced interparticle distances are formed. This results in the formation of defect-sites and gaps within the rafts *(b+e)*. The overall effect is that isolated islands shrink, as do thin bridging structures (figure 1*c+f*). For voids in the structures the opposite occurs and their apparent size increases *(b+e)*.

To illustrate the humidity dependent structural changes, it is instructive to measure the surface area of small islands of particles as well as that of the naturally occurring voids within the rafts of particles. Figure 1*g+h* shows the relative change in size in a range of voids (yellow) and islands (blue) from hydrated to dry. While the voids increase in area size upon drying, the area of the islands decreases. This is consistent with the general tendency of the

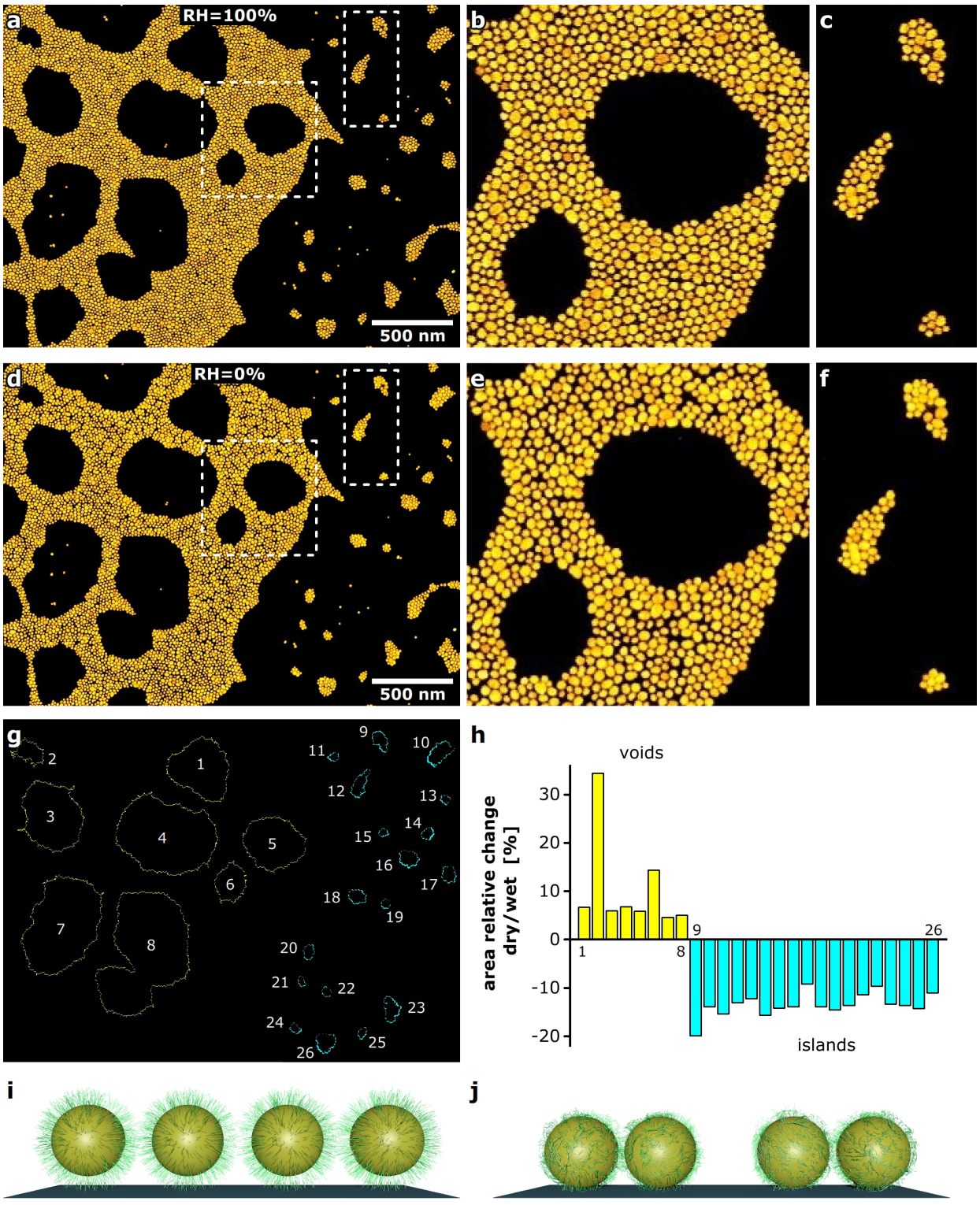

Figure 1: False-colored dark field WetSTEM images showing GNP thin-films under wet (a-c) and dry conditions (d-f). Images b+c (from a) and e+f (from d) are digitally zoomed (3x). The colored outlines (g) show differences in features' sizes between dry and wet condition, with yellow being a positive value (corresponding to enlargement of the voids during drying, numbered 1 to 8) and blue being a negative value (corresponding to shrinkage of islands during drying, numbered 9 to 26). Histogram (h) is showing relative change in area for each feature. (i,j) GNP model showing conformational change in the PEG molecules upon dehydration.

interparticle spacing to decrease upon drying. It should be noted that the same behavior was seen all over the sample, regardless whether a particular area had previously been exposed to the electron beam during imaging in wet conditions. This observation rules out the electron beam irradiation as the driving force behind the observed phenomena. What is more, our experiments showed that a prolonged beam exposure lead to a local pinning of the GNP film, in contrast to the behavior recorded using minimal electron irradiation.

For comparison, similar investigations have been conducted on very monodisperse 17 nm GNP and similar effects were found (see figure SI2 in SI). This supports the notion that the observed changes in particle spacing are not simply an effect of polydispersity and size miss-match within the packed clusters.

To quantify the changes in interparticle distances, software line-scans were performed on a range of the individual islands deliberately selected to be single grain, i.e. without cracks formed upon drying. Figure 2 shows two normalized linescans obtained from the WetSTEM images in figure 1, across the island marked "18", for both dry and hydrated conditions. From a number of such line scans we can estimate an increase in average interparticle spacing of 1.8 nm $\pm$ 0.5 nm upon hydration. Based on FFT analysis of TEM images of rafts of monodisperse GNP (stabilized by the same PEG ligand) under ultra high vacuum (UHV) conditions we know that the interparticle distance in the dry state is 4 nm (see figure SI3 in SI). This means that the interparticle spacing changes from 4 nm in the dry state to 5.8 nm $\pm$ 0.5 nm in the hydrated state. These values will be of interest when discussing the optical and electrical responses of the material. We have recently determined ligand shell thicknesses of comparable materials using differential centrifugal sedimentation (DCS).[52] According to these studies, the particles used here have an estimated ligand shell thickness of approximately 3 nm. This means that in the dry state, there has to be a significant interdigiation of ligands between adjacent particles to enable an average interparticle spacing of 2 nm. This is well known in alkane-thiol stabilized particles.[53] In the hydrated state the distance measurement by WetSTEM correlates well with the ligand shell thickness inferred from DCS

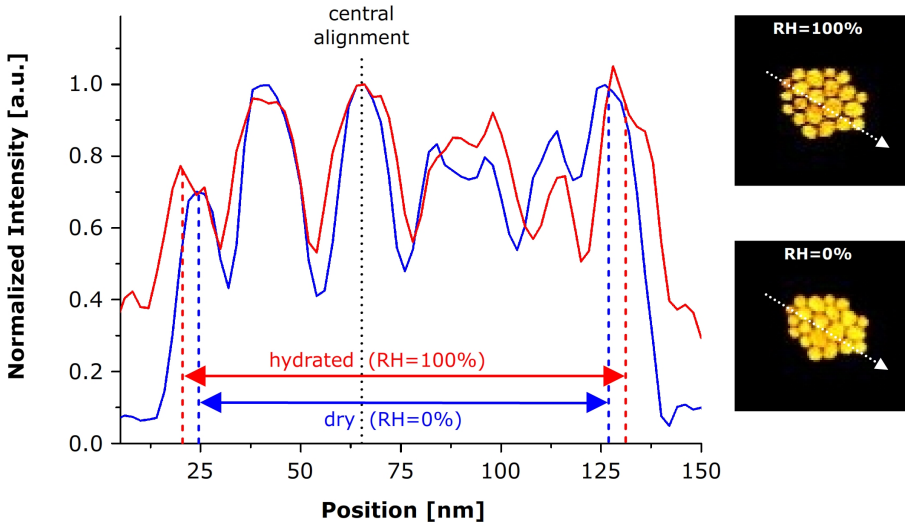

Figure 2: Linescans across island containing six GNPs (feature "18" in figure 1), showing a clear shift (total of 6 nm) in peak position. Normalized around central peak (dashed line).

studies.

We thus interpret the increase/decrease in interparticle distance upon hydration/dehydration as a reversible interdigitation of the hydrophilic PEG ligands (see figure 1i+j). Upon dehydration the more closely packed particles form clusters which are separated from each other by noticeable cracks that account for the shrinkage of interparticle space. The role of the water appears to be to hydrate the individual PEG strands which introduces a slip-zone that makes interdigitation less favorable compared to the dehydrated state. This is in line with previous interpretations of GNP based artificial nose type devices[8,9,11,12] and represents the first direct observation of this effect under fully hydrated conditions. A real-time movie of the drying process can be found in the SI (ESIV1).

While resolution is better in transmission (WetSTEM) mode, this limits the choice of substrates significantly and is therefore not very representative of the samples investigated outside the STEM. It is well known that many ordered structures of nanoparticles form preferentially on the amorphous carbon substrates typically used as TEM sample holders. To exclude that the observed phenomena are specific to this type of substrate, we also conducted

an investigation on native-oxide covered silicon, a typical substrate in device fabrication with similar surface properties to glass.[49] By using ESEM mode it is perform such an investigation, while still utilizing the full range of RH. Figure 3 shows ESEM images obtained on a almost fully hydrated surface (92% RH), where some areas are wet and other remain relatively dry. The images in figure 3 show a transition from a wet to dry part of the sample, clearly in-

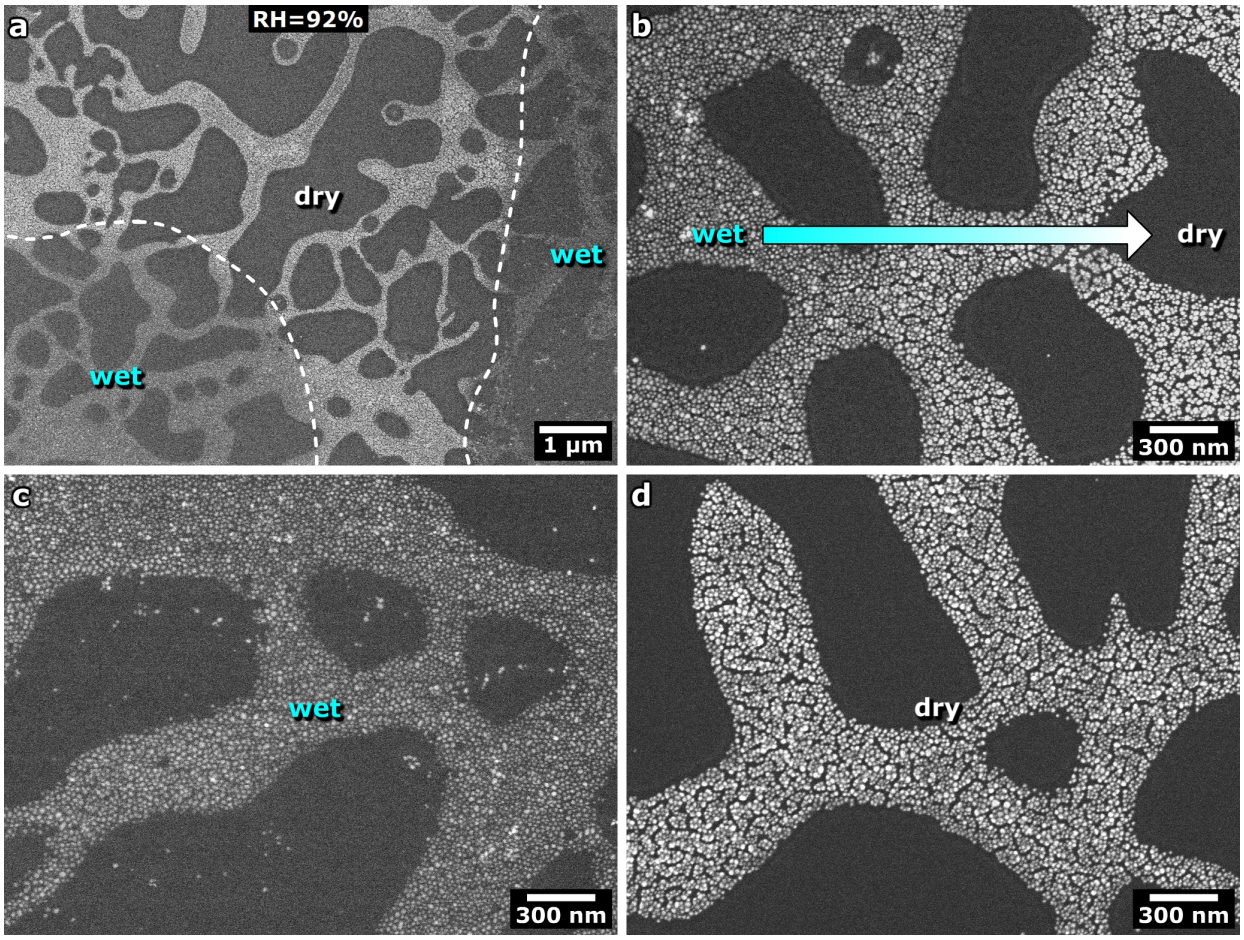

Figure 3: ESEM investigation of GNP assemblies on a partially hydrated (RH = 92%) silicon surface. a) Overview of the GNP structures. b) Transition region between wet and dry area. c) Fully hydrated region, evident from the even particle distribution and slight reduction in contrast due to presence of water. d) Dry region, evident from the cracks in the GNP structure and shorter interparticle distance.

dicated by the change in interparticle distance (especially the cracks in the bulk structure are obvious). Comparing the image in $3c$ and $3d$ the structural difference are clearly seen. This confirms that the effect observed in WetSTEM on a hydrophobic carbon-surface also

appears on hydrophilic silicon, suggesting that the drying behavior is indeed dominated by the ligand-coated GNP, and not by the nature of the substrate.

Optical response

While dispersions of GNP in ethanol (and water) are ruby red, films painted from them appear blue when dried under ambient conditions (see figure 4*a* insert). This is typically observed for a vast range of gold nanoparticle preparations and indicates that the particles aggregate and are in close proximity to each other in the dry deposits.[38] As previously reported by other groups for organic vapor sensors,[29–31] in our samples, the transition from red to blue upon drying is fully reversible. This is comparatively rare since most structural transitions of this type are irreversible. It is sufficient to carefully blow on the film to change its color back to red for the short moment the film remains hydrated (see inset figure 4*b* and video ESIV2 in SI).

To investigate this property further, a sample was drop cast onto a microscope slide and imaged under an optical microscope (see figure 4). The images in figure 4 *left* show the

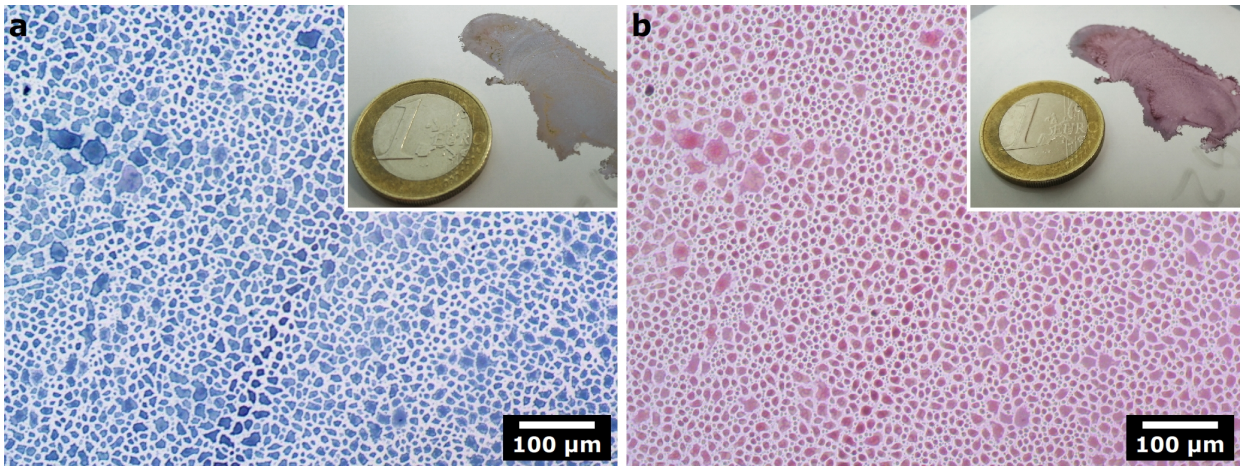

Figure 4: Optical microscope images of a dry sample (ambient conditions) (a) and hydrated sample (b), obtained at 10× magnification. Insets show photographs of a macroscopic droplet painted on a white metallic surface in dry and hydrated states, respectively.

distinct blue color of a dry film (at ambient conditions) with large GNP assemblies clearly visible. Figure 4 *right* show the same sample hydrated, changing its color to red. Upon

closer investigation it is observed that the color change effect is localized, as seen in figure 5*a*, which is obtained as the sample dries again. Comparing this optical microscope image to an ESEM image obtained under similar humidity conditions (figure 5*b*+*c*), the localized effect is also clearly visible. As the sample is hydrated, water droplets form on the surface[49] which slightly changes the interparticle spacing in these regions (as is visible in figure 3*c*). This change in GNP packing changes the optical properties locally and can therefore account for the change in color observed in the optical microscope (see video ESIV3 in SI). The large clusters observed in the optical microscope is an effect of solvent evaporation and depends on both ligand and surface hydrophobicity.[49]

We attribute this local change in color to a ligand-imposed interparticle spacing (see figure 1*i*+*j*), which varies with hydration within the narrow range in which the perceived color is strongly dependent on the spacing. This phenomenon has been studied in great details by Mulvaney *et al.*[22] To quantify the effect and to compare with Mulvaney's set of results we obtained UV/VIS spectra of our films under controlled humidity conditions.

This is done by using a fiber-optical spectrometer connected to a small closed chamber in which the RH can be controlled. A 10 μL sample is drop cast onto a microscope slide and placed on cuvette holder inside the chamber. A white light source is used to illuminate the sample and absorption is measured using the spectrometer. Initial testing show no change in absorption spectra below 80% RH and then a gradual shift of the peak as the RH increases. Starting from standard conditions (room temperature and RH), the sample chamber is slowly filled with water vapor to increase the RH and absorption spectra are obtained continuously. All spectra show a clear absorption peak indicative of the plasmon resonance, although water condensation makes values at really high RH ($> 97\%$) hard to measure reliably due to attenuation. In all spectra, the peak position is recorded and figure 6 show the peak position as a function of measured RH for a full hydration and dehydration cycle. The observed sharp drop ($\approx 95\%$) is due to condensation of water in the film, which is a typical nucleation phenomenon, while the relatively gradual increase ($\approx 80\%$) in peak position with decreasing

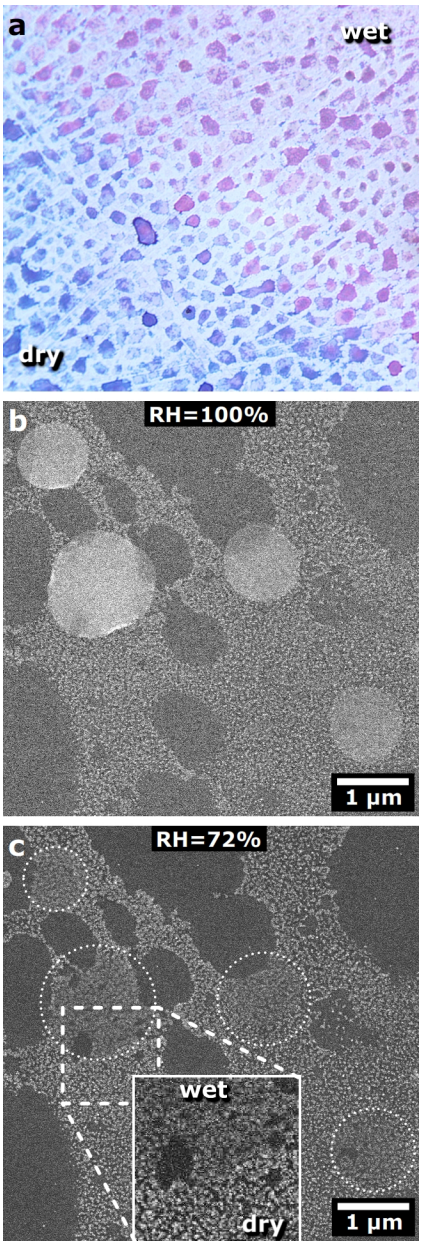

Figure 5: a) Optical microscope image obtained at 20× magnification, showing sample half dry and half wet. b) ESEM image obtained at 100% RH, showing water droplets forming on the surface of a silicon sample. c) Same surface in the following drying cycle, at 72% RH, with hydrated areas indicated by dashed circles, corresponding to the locations of the water droplets condensed in the previous hydration cycle. Inset shows the close-up, emphasizing the structural difference between wet and dry areas.

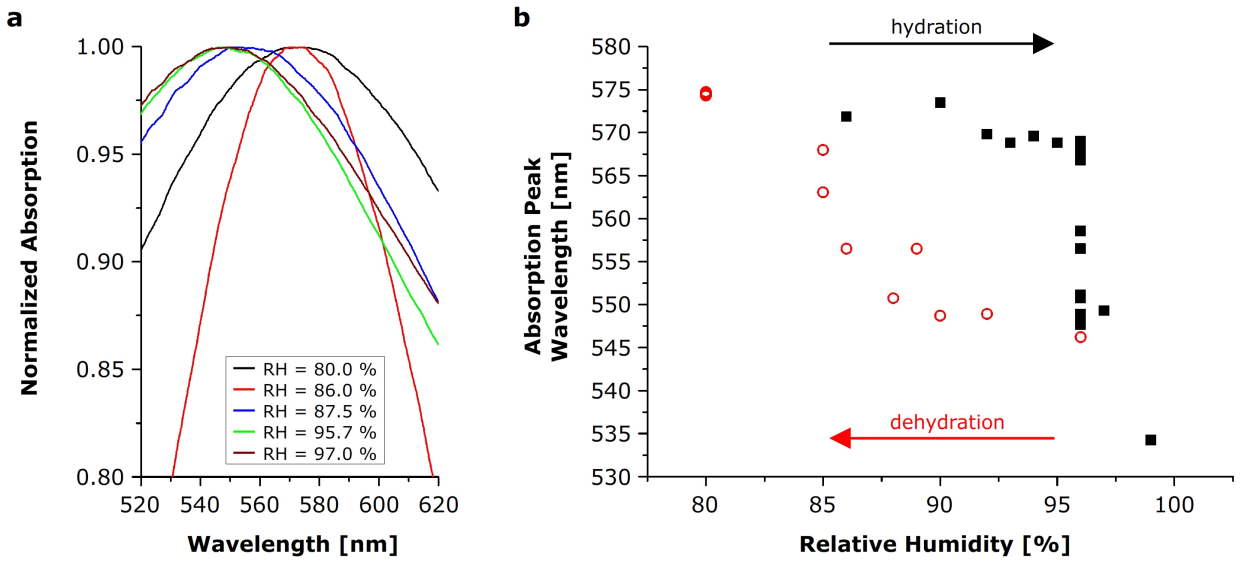

Figure 6: a) Selected absorption peaks (normalized) showing the incremental shifts towards shorter wavelengths with increasing humidity. b) Absorption peak position as a function of measured RH during hydration (black squares) and dehydration cycle (red circles).

RH, is attributed the gradual drying of the film. This behavior is the source of a significant hysteresis in the wetting and drying cycles. Note that water condensation also makes it hard to obtain reliable RH values above 95%. Using this method, a total peak shift of 40 nm (from 575 nm to 535 nm) is measured using the humidity chamber.

To investigate sample reversibility and reproducibility, a sample is cycled 20 times from dry to fully hydrated (in the microscope) and absorption measured (at both dry and hydrated conditions). The plot in figure 7*a*, show all 41 normalized absorption spectra. The two set of peaks clearly indicate a complete reversibility of the system between hydrated and dry conditions and reveal an average peak shift of 45 nm $\pm$ 5nm.

Microscope images are obtained after each drying step in the cycling experiment (see figure 7*b* and animation ESIA4 in SI) and reveal that the local film structure has changed significantly. This is in correspondence with earlier findings that reveal microscopical structure changes in GNP thin films in ESEM where whole clusters of GNP are observed to "float" on wet sample surfaces.[49]

The position of the plasmon absorption peak depends on the refractive index in which plas-

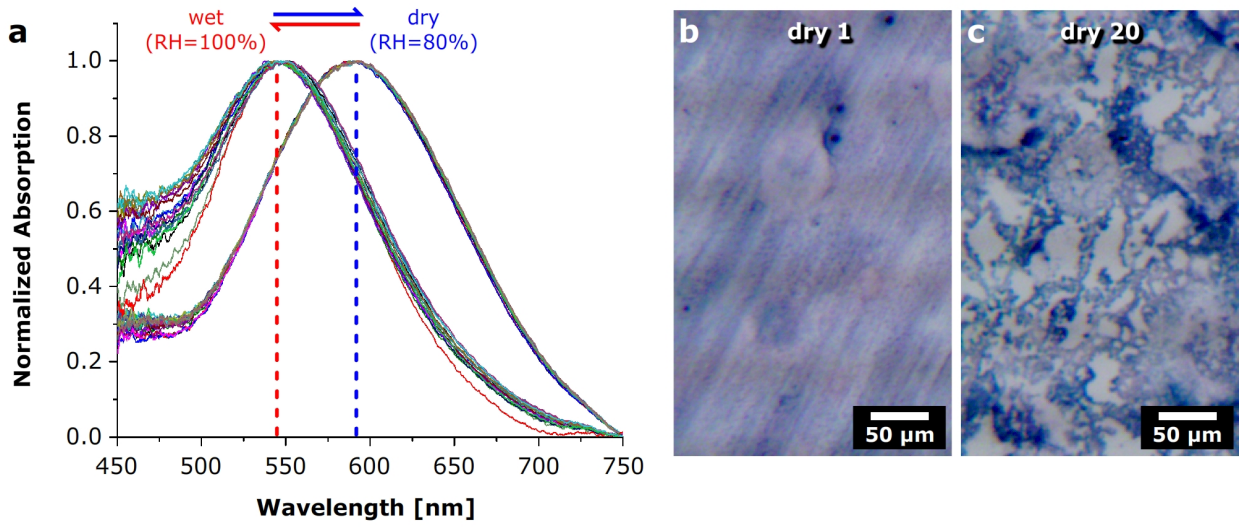

Figure 7: a) 41 normalized absorption spectra for the 20 hydration cycles, showing strong reproducibility. b) Optical microscope image of a dry sample before hydration (*dry 1*) and after 20 hydration cycles (*dry 20*).

monic structures are embedded. Higher values of the refractive index lead to a shift of the position of the plasmon band to longer wavelengths.[54–56] The shift of the plasmon band shown in figure 7 is in the opposite direction indicating that the change in particle spacing upon drying overcompensates the effect of change in refractive index.[22,57–59] This is coherent with previous reports where relatively small changes in the interparticle distance lead to plasmon peak shifts in the range of tens of nanometers.[58,60–64]

Mulvaney and coworkers have clearly demonstrated in a combined experimental and computational study that for films of regularly spaced monodisperse spherical gold nanoparticles with filling factors of 0.5 or smaller the optical properties are well predicted by the established Maxwell-Garnett model, which is based on Mie theory for isolated particles within a homogeneous matrix but takes into account the effective medium due to the proximity of particles within the film.[22] Achieving unprecedented control over all key parameters Mulvaney *et al.* used films formed by highly uniform Au@SiO2 core-shell nanospheres where the well-defined thickness of the silica shell controlled the interparticle spacing and hence the volume fraction occupied by the gold cores. Our films are very similar in structure and appearance except for a moderate polydispersity and a variable interparticle spacing that

is controlled by the degree of hydration of the polymer shell. Rather than attempting to model the optical properties of the films from first principles, we can thus conveniently compare our results with those reported in Mulvaney's study. Upon hydration, the interparticle spacing of our films increases by about 2 nm from 4 nm in the dry state to nearly 6 nm in the fully hydrated state. This results in a 40 nm shift of the plasmon band, from 575 nm to 535 nm (see figure 7). In comparison, Mulvaney reports a shift of 35 nm from 560 nm to 525 nm upon a change in particle spacing by 4 nm from 3 to 7 nm. This is a good agreement bearing in mind that our particles are somewhat bigger and less uniform and that our films may therefore have a filling factor slightly above 0.5, i.e. at the validity limit of the Maxwell-Garnett model. In addition, we have no precise control over the thickness of our drop-cast films, and Mulvaney's work also shows that the position of the plasmon band depends not only on the interparticle spacing, but also on the absolute thickness of the film. Our finding of a marginally more pronounced distance dependence of the optical properties can be accounted for by these differences.

Electrical response

The conductivity of the films deposited on an interdigitated electrode (IDE) array was characterized in two different ways. The first consisted in a simple two-point measurement of the DC resistance using a standard multimeter, and the second in a detailed AC impedance analysis. Most conclusions can be drawn directly from the DC measurement.

Under ambient conditions (45-50% RH) the average resistance based on 15 measurements across 3 IDE's, was 720 Ω. These values increased under fully hydrated conditions (100% RH) to an average of 2600 Ω. The average increase due to hydration is a factor of 3.8, with a standard deviation of 1.1. The averages mask some variation attributed to inconsistencies in film structure following drop casting. The values for each IDE are shown in table 1.

Recovering the conductivity from the measured resistance of an IDE is slightly more involved than for simple geometries. The specific conductivities of the GNP films were therefore deter-

Table 1: IDE resistance data.

IDE	R (ambient) [Ω]	R (100% RH) [Ω]	Increase
A	719 ± 89	2400 ± 300	3.3×
B	405 ± 90	2100 ± 400	5.2×
C	994 ± 74	3160 ± 500	3.2×

mined by both finite-element simulation and analytically[65] (see details and figure SI5 in the SI). This yielded values of 0.12 S/m for ambient conditions and 0.032 S/m when hydrated. These values were generated by the simulated model, and were 20% higher than those predicted by the analytical solution. This is because the analytical solution fails to take into account potential drops along the digits of the electrode, which were significant due to the extreme aspect ratio of the digits (1:1340), and the relative conductivity of the films. These numbers are higher than many previously reported values for GNP films.[2,10,65,66] However, it is known that subtle variations of film compositions can lead to changes in conductivity over many orders of magnitude. We attribute the high conductance of our GNP films predominantly to the metal core size of our particles which is about ten times that of most reported materials. This implies that the gold content of our films by volume is four to six times higher than that of films made with significantly smaller particles. In addition we would not expect coulomb blockade effects which in the case of much smaller particles can impede charge separation and hence electron transfer. With respect to the decrease in conductivity upon hydration, several groups[41,43,67] have confirmed that shorter carbon-chains, as expected, lead to higher conductivity. An increase in conductivity up to 7 orders of magnitude has been reported when decreasing the chain length from C9 to C3.[43] In comparison, our variability of interparticle spacing based on PEG swelling upon hydration, is relatively small, but still gives rise to significant change in conductivity. It is known that interparticle spacing also has an effect on the activation energy for charge hopping, however for larger particles such as ours, the effect on conductivity should be negligible, on the order of 2%.[68] With a binary data set (hydrated/ambient) it is not possible to, as others have done,[2,65] fit separation vs conductivity to demonstrate the exponential decay expected for tunneling/hopping mecha-

nisms.

It should be noted that, an opposite effect, *i.e.* an increase in conductivity upon hydration has been reported previously[66] using short-chain hydrophobic ligands, hence we would not expect the swelling effect presented here. Nevertheless, an increase in conductivity upon hydration can also be observed in our films if the measurement is taken a significantly larger area so that microscopic cracks compromise the continuity of the films (see SI for details). In this case dry films show practically no conductance whereas hydrated films do conduct due to the "healing" of the cracks (observed in the WetSTEM images (see figure 3)). The results obtained on the IDE should be seen as equivalent to measuring the electrical properties of the unfractured islands shown in figure 3.

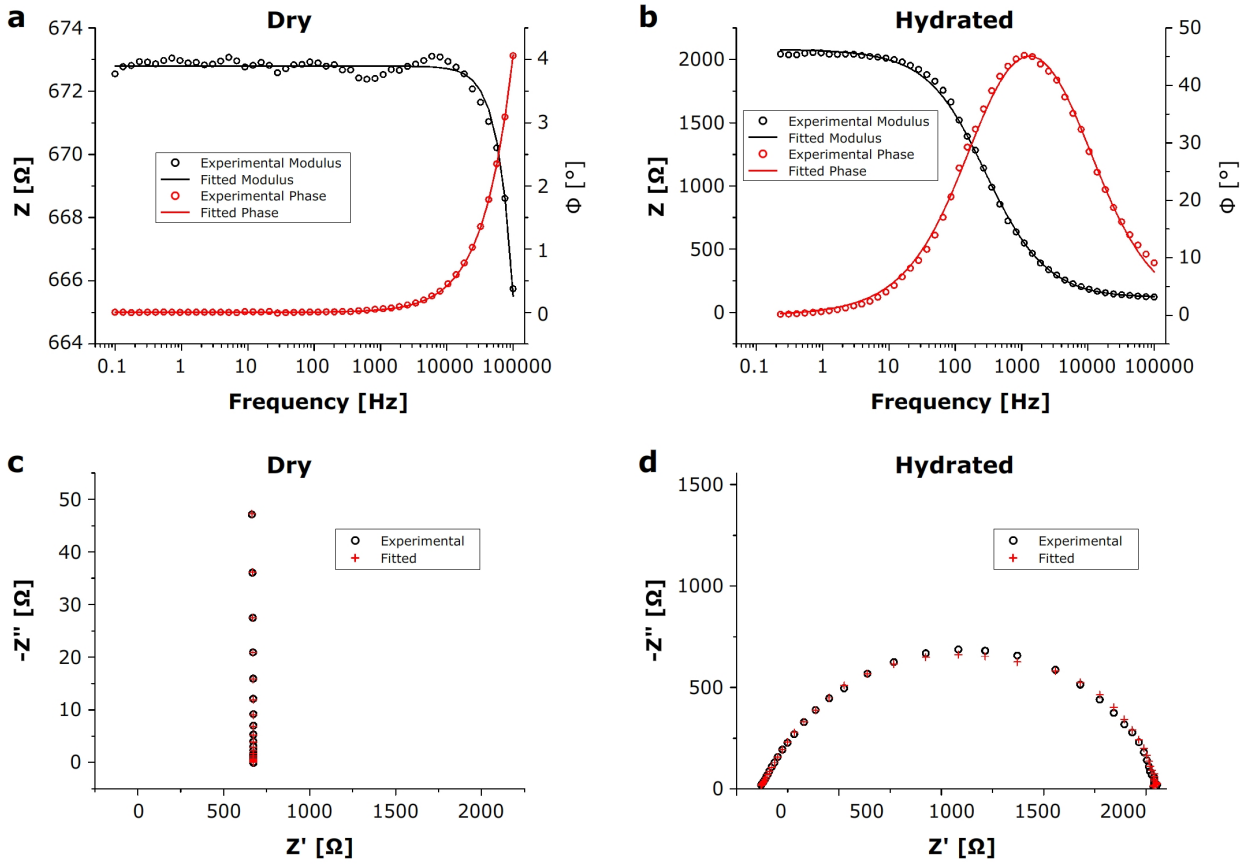

Figure 8: Impedance analysis of dry *(left)* and fully hydrated *(right)* GNP films on interdigitated electrodes (Bode plots *top* and Nyquist plots *bottom*).

The results of the AC impedance measurements are presented in figure 8. As recently shown

by Rotello and coworkers, the AC impedance of the dry samples can be interpreted in terms of a resistor and a capacitor in parallel.[69] Even a single resistor gives a very good fit up to a frequency of about 10.000 Hz indicating that the capacitance of the dry films is very small indeed. The hydrated samples, in contrast, show an influence of the capacitance already at 10 Hz but are generally better fitted by replacing the capacitor with a so-called constant phase element (CPE) (see figure SI4 in SI for comparison). While there is no physical equivalent of a CPE it can be represented by an extended array of different RC circuits in parallel. This system is widely used in the electrochemical literature to account for heterogeneity in electrode surfaces analyzed by impedance techniques.[70] In our case, polydispersity and packing irregularities will cause disparate hopping paths and a range of capacitive gaps to exist within the film . Upon hydration the resistance of the films increases from 670 to 2000Ω, in line with the results of the prior DC experiment, while the capacitance increases by three orders of magnitude (1 nF to 1 μF). Both changes are qualitatively congruent with the expectations based on the measured change in interparticle spacing and the estimated change in matrix dielectric constant upon hydration of the matrix. No evidence of a diffusive mechanism for charge transfer was observed at any humidity level. This effect has been reported for the hydration of bare nanoparticle films[71] and is characterised by a linear tail on the Nyquist plots (Warburg impedance). It is, therefore, proposed that conductance in our films is achieved solely through a hopping mechanism, as no Warburg impedance is evident in figure 8.

Conclusions

The very small changes in interparticle spacing in GNP films caused by swelling of the hydrophilic ligand shell upon hydration have been measured *in-situ* by electron microscopy under ambient conditions. Corresponding changes in optical properties were quantified and in full agreement with the expectations based on the structural changes. Changes in electri-

cal conductance were interpreted qualitatively by a combination of structural changes and the difference in dielectric constant of the matrix upon hydration. Consequently, hydrated films behaved electrically more like a resistor and a capacitor in parallel, while dry films could be regarded approximately at pure resistors. This report contributes to a better mechanistic understanding of ambient sensing and medical diagnostics by nanostructured thin film devices.

Experimental

Particle Synthesis

Batches of gold nanoparticles typically in the 19 nm range,[49] were prepared following the classic Turkevich citrate reduction method.[72] Briefly, 86 mg of *hydrogentetrachloroaurate trihydrate* ($HAuCL_4 \times 3H_2O$, Sigma Aldrich) was dissolved in 140 ml of DI water and brought to boil in a round bottom flask equipped with a reflux condenser. Then 20 ml of a near boiling hot aqueous solution of trisodium citrate (0.9 mM) was added rapidly through the condenser under vigorous stirring, and the mixture was refluxed for 30 min. After cooling the mixture down to room temperature, 13.6 mg (17 μMol) of *mercaptopolyethylenglycol* (PEG) polymer (MW: 800 g/mol) was added and dissolved by vigorous shaking of the flask. The mixture was allowed to react overnight and excess polymer was removed by repeated centrifugation and re-dispersion of the particles in water until frothing (due to excess surfactant) was no longer observed upon vigorous shaking of the dispersion. The dispersions are stable at least for several months and the particles do not sediment even after prolonged storage without agitation.

Typically batches of GNP prepared in this way vary in monodispersity. Most measurements were obtained from moderately monodisperse samples. Control experiments using a sample of exceptional monodispersity, did not lead to significant differences, except for the ability to obtain exact interparticle spacings of dry samples by FFT of TEM images.

Electron Microscopy

All scanning electron microscopy imaging was conducted using a FEI *Quanta 250* FEG Scanning Electron Microscope (SEM), operated in either ESEM or WetSTEM mode for reaching "above-zero" humidity conditions, or in high vacuum mode (pressure in 10^{-4}Pa range) for "zero" humidity conditions.

This microscope has a sample chamber which utilizes differential pumping, allowing for samples to be held at pressures of up to 2700 Pa. The chamber is equipped with a Peltier cooling stage and can be filled with pure water vapor. By adjusting temperature and pressure, according to the water phase diagram of water, complete humidity control is possible, so that fully hydrated (100% RH) samples can be imaged. This was utilized in both modes. In WetSTEM mode full beam acceleration was used (30kV), while only moderate energy was used in ESEM (10kV). In both cases a spot size of 2.5 was used. For WetSTEM, samples were deposited on a **copper** TEM grid (Agar Scientific), covered with an amorphous carbon thin film. In ESEM a Si surface was used. A 4×4 mm wafers cut from a n-doped silicon [100] wafer was cleaned with acetone and ethanol in a sonicator for 15 min in each solution and dried using Argon. These Si surfaces are normally covered with native oxide (around 1 nm)[73] and are quite hydrophilic (contact angle $< 20°$).[74]

Electron microscopy images were analyzed using ImageJ. Special care was taken to minimize image processing (in particular, image contrast and brightness adjustment), to avoid any misinterpretation that might arise from image "overprocessing". For that reason, the images were used as raw as possible, apart from applying color scheme in WetSTEM images.

While an electron beam can be used in many interesting ways to pattern surfaces,[75,76] SEM imaging is also known to to have a range of effects on the examined surface. For instance, it can affect the surface wettability, particle properties, induce surface heating, and even create free radicals.[77–81] Therefore, great care was taken to keep the beam energy and electron dose as low as possible (while still maintaining good image quality), in line with the methodology of Rykazcewski and coworkers.[82,83] Furthermore, frequent periods of beam-blanking were en-

forced to allow for dissipation of built up surface charge. See figure SI7 for images indicating that the observed effects are not beam induced damage.

In accordance with previous work, similar protocols were followed to hydrate sample surfaces.[49] For hydration experiments the sample was slowly dehydrated in the SEM chamber to around 10% RH (200 Pa at 2°C) and the water vapor pressure was then slowly increased to the dew-point and beyond, while surface features were continuously imaged. This method was followed for both ESEM and WetSTEM modes.

Ex-situ TEM imaging was conducted on an FEI Tecnai T12 Spirit microscope operating at an accelerating voltage of 120 kV.

In total for the results presented in this paper, we had spent 29 full-day ESEM sessions over the course of 11 months. In total, more than 70 samples were prepared by drop-cast deposition of GNPs on various substrates. All three vacuum regimes that the microscope can operate in (ESEM, low-vacuum, high vacuum) had been utilized in our investigation. Based on the results of our extensive study, we found that the clearest visualization of GNP self-assembly upon drying/wetting was achieved using dark-field WetSTEM at 30.000 to 100.000 × magnification, having the GNP deposited on amorphous carbon film (i.e. TEM grids). Typically, in this way, only 1 to 2 samples undergoing multiple wet-dry transitions would be examined during a full-day session. Overall, approximately 20 WetSTEM samples were prepared and investigated; out of that, 8 samples were examined more thoroughly due to favorable appearance, with more than 60 spots (i.e. regions of interest) imaged in detail. Virtually all of the images reveal the same behavior of GNPs during hydration/dehydration, albeit at various clarity/quality/resolution, strongly indicating that the findings are statistically very relevant. The micrographs presented in the manuscript were selected on the basis of their clarity and are very representative of the generally observed behavior. In total, more than 2300 images of GNP hydration/dehydration assemblies were acquired, including 336 pairs of bright-field/dark-field WetSTEM images, as well as 39 movies. In addition, 235 bright-field TEM images of 7 samples were obtained during 5 TEM sessions.

Optical Spectroscopy

Images are obtained using a fluorescence microscope (Brunel SP300F) equipped with a CCD camera (UCMOS 5100 KPA) and 10×, 20×, 40× and 100× microscope objectives.

Spectroscopic data are obtained using a spectrometer (Ocean Optics USB4000), connected to a white light halogen source (Ocean Optics HL-2000-FHSA). Both light source and spectrometer is connected to either side of a fiber-optic cell using multimode fibers and absorption is measured in transmission mode through a glass objective slide with sample deposited on the front side.

The humidity chamber consists of a 50 mm diameter glass tube (length 25 cm) containing a digital humidity sensor (Will Hi WH8040) and the fiber-optic cell. The chamber is connected to a hotplate with boiling water (Millipore, MilliQ+ 185) into which Argon (Standard grade pure, BOC) gas flows. By adjusting the Ar flow, the chamber humidity is controlled.

Electrical Characterization

The electrical properties of the particles were assessed by drop-casting a thin film, from ethanol, onto interdigitated platinum electrodes deposited on glass (Dropsense, G-IDEPR5). The electrode contains 2 × 250 digits, each 5 μm wide and with 5 μm spacing (total digit length 6760 μm). Thickness of the GNP film is hard to estimate from a drop cast solution, but from the SEM images is estimated to be just a single monolayer. Resistance measurements were performed using a multimeter (Fluke, CNX 3000) and a potentiostat equipped with a frequency response analysis module (MetroHM, PGSTAT302N + FRA32M) which also provided the impedance analysis. The clean interdigitated electrodes had a dry resistance >50MΩ (and 3MΩ at 100% RH). Fitting of impedance data to equivalent circuit responses was achieved using simulation software (MetroHM, Nova 1.11).

Hydration was achieved by passing a stream of air saturated with water (Millipore, MilliQ+ 185) across the electrode surface. Zero humidity was prepared by sealing the electrode in a plastic tube (Vulcan Centrifuge) with desiccant (Sigma, silica gel).

Acknowledgement

Funding from the European Research Council (ERC) via the Advanced Grant "PANDORA" is gratefully acknowledged. We would also like thank Volfango Bertola (Dept. of Engineering, University of Liverpool), for assistance with humidity chamber and A. Beckett and I. Prior from the Biomedical Electron Microscopy Unit, University of Liverpool.

Supporting Information Available

Supporting Information Available: Animations and videos obtained in WetSTEM mode illustrating swelling and shrinking of GNP assemblies upon hydration and drying. TEM images used for GNP size distribution and FFT analysis. Comparative fitting of the obtained impedance spectroscopy data for hydrated samples. SEM images of IDE structure with GNP thin film. Simulated results used to obtain specific conductivity for GNP thin films.

This material is available free of charge via the Internet at `http://pubs.acs.org/`.

References

1. Brust, M.; Walker, M.; Bethell, D.; Schiffrin, D. J.; Whyman, R. Synthesis of Thiol-Derivatised Gold Nanoparticles in a Two-Phase Liquid-Liquid System. *J. Chem. Soc., Chem. Commun.* **1994**, 801–802.

2. Templeton, A. C.; Wuelfing, W. P.; Murray, R. W. Monolayer-Protected Cluster Molecules. *Acc. Chem. Res.* **2000**, *33*, 27–36.

3. Daniel, M.-C.; Astruc, D. Gold Nanoparticles: Assembly, Supramolecular Chemistry, Quantum-Size-Related Properties, and Applications toward Biology, Catalysis, and Nanotechnology. *Chem. Rev.* **2004**, *104*, 293–346.

4. Zhao, P.; Li, N.; Astruc, D. State of the Art in Gold Nanoparticle Synthesis. *Coord. Chem. Rev.* **2013**, *257*, 638–665.

5. Persaud, K.; Dodd, G. Analysis of Discrimination Mechanisms in the Mammalian Olfactory System Using a Model Nose. *Nature* 352–355.

6. Freund, M. S.; Lewis, N. S. A Chemically Diverse Conducting Polymer-Based "Electronic Nose". *Proc. Natl. Acad. Sci. U.S.A.* **1995**, *92*, 2652–2656.

7. Wohltjen, H.; Snow, A. W. Colloidal Metal-Insulator-Metal Ensemble Chemiresistor Sensor. *Anal. Chem.* **1998**, *70*, 2856–2859.

8. Vossmeyer, T.; Guse, B.; Besnard, I.; Bauer, R.; Müllen, K.; Yasuda, A. Gold Nanoparticle/Polyphenylene Dendrimer Composite Films: Preparation and Vapor-Sensing Properties. *Adv. Mater.* **2002**, *14*, 238–242.

9. Vossmeyer, T.; Joseph, Y.; Besnard, I.; Harnack, O.; Krasteva, N.; Guse, B.; Nothofer, H.-G.; Yasuda, A. Gold-Nanoparticle/Dithiol Films as Chemical Sensors and First Steps Toward Their Integration on Chip. *Proc. SPIE* **2004**, *5513*, 202–212.

10. Wessels, J. M.; Nothofer, H.-G.; Ford, W. E.; von Wrochem, F.; Scholz, F.; Vossmeyer, T.; Schroedter, A.; Weller, H.; Yasuda, A. Optical and Electrical Properties of Three-Dimensional Interlinked Gold Nanoparticle Assemblies. *J. Am. Chem. Soc.* **2004**, *126*, 3349–3356.

11. Steinecker, W. H.; Rowe, M. P.; Zellers, E. T. Model of Vapor-Induced Resistivity Changes in Gold-Thiolate Monolayer-Protected Nanoparticle Sensor Films. *Anal. Chem.* **2007**, *79*, 4977–4986.

12. Joseph, Y.; Guse, B.; Vossmeyer, T.; Yasuda, A. Gold Nanoparticle/Organic Networks as Chemiresistor Coatings: The Effect of Film Morphology on Vapor Sensitivity. *J. Phys. Chem. C* **2008**, *112*, 12507–12514.

13. Snow, A. W.; Wohltjen, H.; Jarvis, N. L. In *Defense Applications of Nanomaterials*; Miziolek, A. W., Karna, S. P., Mauro, J. M., Vaia, R. A., Eds.; ACS Symposium Series; American Chemical Society: Washington, DC, 2005; Vol. 891; Chapter 3, pp 31–45.

14. Olichwer, N.; Leib, E. W.; Halfar, A. H.; Petrov, A.; Vossmeyer, T. Cross-Linked Gold Nanoparticles on Polyethylene: Resistive Responses to Tensile Strain and Vapors. *ACS Appl. Mater. Interfaces* **2012**, *4*, 6151–6161.

15. Doty, R. C.; Yu, H.; Shih, C. K.; Korgel, B. A. Temperature-Dependent Electron Transport through Silver Nanocrystal Superlattices. *J. Phys. Chem. B* **2001**, *105*, 8291–8296.

16. Sigman, M. B.; Saunders, A. E.; Korgel, B. A. Metal Nanocrystal Superlattice Nucleation and Growth. *Langmuir* **2004**, *20*, 978–983.

17. Yu, Y.; Jain, A.; Guillaussier, A.; Voggu, V. R.; Truskett, T. M.; Smilgies, D.-M.; Korgel, B. A. Nanocrystal Superlattices that Exhibit Improved Order on Heating: An Example of Inverse Melting? *Faraday Discuss.* **2015**, *181*, 181–192.

18. Peng, G.; Tisch, U.; Adams, O.; Hakim, M.; Shehada, N.; Broza, Y. Y.; Billan, S.; Abdah-Bortnyak, R.; Kuten, A.; Haick, H. Diagnosing Lung Cancer in Exhaled Breath Using Gold Nanoparticles. *Nat. Nanotechnol.* **2009**, *4*, 669–673.

19. Segev-Bar, M.; Haick, H. Flexible Sensors Based on Nanoparticles. *ACS Nano* **2013**, *7*, 8366–8378.

20. Nakhleh, M.; Broza, Y. Y.; Haick, H. Monolayer-Capped Gold Nanoparticles for Disease Detection from Breath. *Nanomedicine (Lond.)* **2014**, *9*, 1991–2002.

21. Underwood, S.; Mulvaney, P. Effect of the Solution Refractive Index on the Color of Gold Colloids. *Langmuir* **1994**, *10*, 3427–3430.

22. Ung, T.; Liz-Marzán, L. M.; Mulvaney, P. Optical Properties of Thin Films of AuSiO2 Particles. *J. Phys. Chem. B* **2001**, *105*, 3441–3452.

23. Liz-Marzán, L. M. Nanometals. *Mater. Today* **2004**, *7*, 26–31.

24. Li, Z.; Nan, J.; Zhang, X.; Ye, S.; Shen, H.; Wang, S.; Fang, L.; Xue, P.; Zhang, J.; Yang, B. Modulate the Morphology and Spectroscopic Property of Gold Nanoparticle Arrays by Polymer-Assisted Thermal Treatment. *J. Phys. Chem. C* **2015**, *119*, 11839–11845.

25. Liz-Marzán, L. M. Tailoring Surface Plasmons through the Morphology and Assembly of Metal Nanoparticles. *Langmuir* **2006**, *22*, 32–41.

26. Klinkova, A.; Choueiri, R. M.; Kumacheva, E. Self-Assembled Plasmonic Nanostructures. *Chem. Soc. Rev* **2014**, *43*, 3976–3991.

27. Sánchez-Iglesias, A.; Grzelczak, M.; Pérez-Juste, J.; Liz-Marzán, L. M. Binary Self-Assembly of Gold Nanowires with Nanospheres and Nanorods. *Angew. Chem. Int. Ed.* **2010**, *49*, 9985–9989.

28. Xiong, W.; Sikdar, D.; Yap, L. W.; Premaratne, M.; Li, X.; Cheng, W. Multilayered Core-Satellite Nanoassemblies with Fine-Tunable Broadband Plasmon Resonances. *Nanoscale* **2015**, *7*, 3445–3452.

29. Dalfovo, M. C.; Salvarezza, R. C.; Ibañez, F. J. Improved Vapor Selectivity and Stability of Localized Surface Plasmon Resonance with a Surfactant-Coated Au Nanoparticles Film. *Anal. Chem.* **2012**, *84*, 4886–4892.

30. Potyrailo, R. A.; Larsen, M.; Riccobono, O. Detection of Individual Vapors and Their Mixtures Using a Selectivity-Tunable Three-Dimensional Network of Plasmonic Nanoparticles. *Angew. Chem. Int. Ed.* **2013**, *52*, 10360–10364.

31. Chen, F.-Y.; Chang, W.-C.; Jian, R.-S.; Lu, C.-J. Novel Gas Chromatographic Detector Utilizing the Localized Surface Plasmon Resonance of a Gold Nanoparticle Monolayer inside a Glass Capillary. *Anal. Chem.* **2014**, *86*, 5257–5264.

32. Giner-Casares, J. J.; Liz-Marzán, L. M. Plasmonic Nanoparticles in 2D for Biological Applications: Toward Active Multipurpose Platforms. *Nano Today* **2014**, *9*, 365–377.

33. Mirkin, C. A.; Letsinger, R. L.; Mucic, R. C.; Storhoff, J. J. A DNA-Based Method for Rationally Assembling Nanoparticles into Macroscopic Materials. *Nature* **1996**, *382*, 607–609.

34. Elghanian, R.; Storhoff, J. J.; Mucic, R. C.; Letsinger, R. L.; Mirkin, C. A. Selective Colorimetric Detection of Polynucleotides Based on the Distance-Dependent Optical Properties of Gold Nanoparticles. *Science* **1997**, *277*, 1078–1081.

35. Storhoff, J. J.; Elghanian, R.; Mucic, R. C.; Mirkin, C. A.; Letsinger, R. L. One-Pot Colorimetric Differentiation of Polynucleotides with Single Base Imperfections Using Gold Nanoparticle Probes. *J. Am. Chem. Soc.* **1998**, *120*, 1959–1964.

36. Sönnichsen, C.; Reinhard, B. M.; Liphardt, J.; Alivisatos, A. P. A Molecular Ruler Based on Plasmon Coupling of Single Gold and Silver Nanoparticles. *Nat. Biotechnol.* **2005**, *23*, 741–745.

37. Wang, Z.; Lévy, R.; Fernig, D. G.; Brust, M. Kinase-Catalyzed Modification of Gold Nanoparticles: A New Approach to Colorimetric Kinase Activity Screening. *J. Am. Chem. Soc.* **2006**, *128*, 2214–2215.

38. Wilson, R. The Use of Gold Nanoparticles in Diagnostics and Detection. *Chem. Soc. Rev.* **2008**, *37*, 2028–2045.

39. Park, J.; Zheng, H.; Lee, W. C.; Geissler, P. L.; Rabani, E.; Alivisatos, A. P. Direct Observation of Nanoparticle Superlattice Formation by Using Liquid Cell Transmission Electron Microscopy. *ACS Nano* **2012**, *6*, 2078–2085.

40. Tanaka, Y.; Matsumoto, A.; Tsuruoka, T.; Nawafune, H.; Akamatsu, K. Gold Nanopar-

ticle Satellite Nanostructures on a Glass Substrate for Dual-responsive Optical Sensing of Organic Liquids. *Chem. Lett.* **2014**, *43*, 1084–1085.

41. Fishelson, N.; Shkrob, I.; Lev, O.; Gun, J.; Modestov, A. D. Studies on Charge Transport in Self-Assembled Gold-Dithiol Films: Conductivity, Photoconductivity, and Photoelectrochemical Measurements. *Langmuir* **2001**, *17*, 403–412.

42. Nitzan, A. Electron Transmission Through Molecules and Molecular Interfaces. *Annu. Rev. Phys. Chem.* **2001**, *52*, 681–750.

43. Pełka, J. B.; Brust, M.; Gierlowski, P.; Paszkowicz, W.; Schell, N. Structure and Conductivity of Self-Assembled Films of Gold Nanoparticles. *Appl. Phys. Lett.* **2006**, *89*, 063110.

44. Wang, G. R.; Wang, L.; Rendeng, Q.; Wang, J.; Luo, J.; Zhong, C.-J. Correlation Between Nanostructural Parameters and Conductivity Properties for Molecularly-Mediated Thin Film Assemblies of Gold Nanoparticles. *J. Mater. Chem.* **2007**, *17*, 457–462.

45. Brust, M.; Schiffrin, D. J.; Bethell, D.; Kiely, C. J. Novel Gold-Dithiol Nano-Networks with Non-Metallic Electronic Properties. *Adv. Mater.* **1995**, *7*, 795–797.

46. Terrill, R. H.; Postlethwaite, T. A.; Chen, C.-H.; Poon, C.-D.; Terzis, A.; Chen, A.; Hutchison, J. E.; Clark, M. R.; Wignall, G. Monolayers in Three Dimensions: NMR, SAXS, Thermal, and Electron Hopping Studies of Alkanethiol Stabilized Gold Clusters. *J. Am. Chem. Soc.* **1995**, *117*, 12537–12548.

47. Stansfield, G. L.; Thomas, P. J. Substituent Effects on Charge Transport in Films of Au Nanocrystals. *J. Am. Chem. Soc.* **2012**, *134*, 11888–11891.

48. Pang, P.; Guo, Z.; Cai, Q. Humidity Effect on the Monolayer-Protected Gold Nanoparticles Coated Chemiresistor Sensor for VOCs Analysis. *Talanta* **2005**, *65*, 1343–1348.

49. Kunstmann-Olsen, C.; Belić, D.; Brust, M. Monitoring Pattern Formation in Drying and Wetting Dispersions of Gold Nanoparticles by ESEM. *Faraday Discuss.* **2015**, *181*, 281–298.

50. Novotný, F.; Wandrol, P.; Proška, J.; Šlouf, M. In Situ WetSTEM Observation of Gold Nanorod Self-Assembly Dynamics in a Drying Colloidal Droplet. *Microsc. Microanal.* **2014**, *20*, 385–393.

51. Verch, A.; Pfaff, M.; de Jonge, N. Exceptionally Slow Movement of Gold Nanoparticles at a Solid/Liquid Interface Investigated by Scanning Transmission Electron Microscopy. *Langmuir* **2015**, *31*, 6956–6964.

52. Krpetić, Z.; Davidson, A.; Volk, M.; Lévy, R.; Brust, M.; Cooper, D. High-Resolution Sizing of Monolayer Protected Gold Clusters by Differential Centrifugal Sedimentation. *ACS Nano* **2013**, *10*, 8881–8890.

53. Wang, Z. L.; Harfenist, S. A.; Whetten, R. L.; Bentley, J.; Evans, N. D. Bundling and Interdigitation of Adsorbed Thiolate Groups in Self-Assembled Nanocrystal Superlattices. *J. Phys. Chem. B* **1998**, *17*, 3068–3072.

54. P.Mulvaney, Surface Plasmon Spectroscopy of Nanosized Metal Particles. *Langmuir* **1996**, *12*, 788–800.

55. Pastoriza-Santos, I.; Sánchez-Iglesias, A.; García de Abajo, F. J.; Liz-Marzán, L. M. Environmental Optical Sensitivity of Gold Nanodecahedra. *Adv. Funct. Mater.* **2007**, *17*, 1443–1450.

56. Fang, Z.; Zhen, Y.-R.; Neumann, O.; Polman, A.; García de Abajo, F. J.; Nordlander, P.; Halas, N. J. Evolution of Light-Induced Vapor Generation at a Liquid-Immersed Metallic Nanoparticle. *Nano Lett.* **2013**, *13*, 1736–1742.

57. Dusemund, B.; Hoffmann, A.; Salzmann, T.; Kreibig, U.; Schmid, G. Cluster Matter: The Transition of Optical Elastic Scattering to Regular Reflection. *Z. Phys. D: At. Mol. Clusters* **1991**, *308*, 305–308.

58. García de Abajo, F. J. Nonlocal Effects in the Plasmons of Strongly Interacting Nanoparticles, Dimers, and Waveguides. *J. Phys. Chem. C* **2008**, *112*, 17983–17987.

59. Halas, N. J.; Lal, S.; Chang, W.-S.; Link, S.; Nordlander, P. Plasmons in Strongly Coupled Metallic Nanostructures. *Chem. Rev.* **2011**, *111*, 3913–3961.

60. Yoon, J. H.; Yoon, S. Probing Interfacial Interactions Using Core-Satellite Plasmon Rulers. *Langmuir* **2013**, *29*, 14772–14778.

61. Cha, H.; Yoon, J. H.; Yoon, S. Probing Quantum Plasmon Coupling Using Gold Nanoparticle Dimers with Tunable Interparticle Distances Down to the Subnanometer Range. *ACS Nano* **2014**, *8*, 8554–8563.

62. Ding, T.; Sigle, D.; Zhang, L.; Mertens, J.; de Nijs, B.; Baumberg, J. Controllable Tuning Plasmonic Coupling with Nanoscale Oxidation. *ACS Nano* **2015**, *9*, 6110–6118.

63. Jiang, N.; Ruan, Q.; Qin, F.; Wang, J.; Lin, H.-Q. Switching Plasmon Coupling through the Formation of Dimers from Polyaniline-Coated Gold Nanospheres. *Nanoscale* **2015**, *7*, 12516–12526.

64. Du, J.; Zhu, B.; Leow, W. R.; Chen, S.; Sum, T. C.; Peng, X.; Chen, X. Colorimetric Detection of Creatinine Based on Plasmonic Nanoparticles via Synergistic Coordination Chemistry. *Small* **2015**, 4104–4110.

65. Foos, E. E.; Snow, A. W.; Twigg, M. E.; Ancona, M. G. Thiol-Terminated Di-, Tri-, and Tetraethylene Oxide Functionalized Gold Nanoparticles: A Water-Soluble, Charge-Neutral Cluster. *Chem. of Mat.* **2002**, *14*, 2401–2408.

66. Lee, H.-C.; Wang, C.-Y.; Lin, C.-H. High-Performance Humidity Sensors Utilizing Dopamine Biomolecule-Coated Gold Nanoparticles. *Sens. Actuators, B* **2014**, *191*, 204–210.

67. Bethell, D.; Brust, M.; Schiffrin, D. J.; Kiely, C. From Monolayers to Nanostructured Materials: An Organic Chemist's View of Self-Assembly. *J. Electroanal. Chem.* **1996**, *409*, 137–143.

68. Brust, M.; Bethell, D.; Kiely, C.; Schiffrin, D. Self-Assembled Gold Nanoparticle Thin Films with Nonmetallic Optical and Electronic Properties. *Langmuir* **1998**, *19*, 5425–5429.

69. Yu, X.; Malvankar, N.; Landis, R.; Eymur, S.; Miranda, O. R.; Rotello, V. M. Impedance Spectroscopy of Ionic Ligand-Modulated Charge Transport of Gold Nanoparticle Films. *Small* **2015**, *11*, 3814–3821.

70. Brug, G. J.; van den Eeden, A. L. G.; Sluyters-Rehbach, M.; Sluyters, J. H. The Analysis of Electrode Impedances Complicated by the Presence of a Constant Phase Element. *J. Electroanal. Chem. Interfacial Electrochem.* **1984**, *176*, 275–295.

71. Thiwawong, T.; Onlaor, K.; Tunhoo, B. A Humidity Sensor Based on Silver Nanoparticles Thin Film Prepared by Electrostatic Spray Deposition Process. *Adv. Mater. Sci. Eng.* **2013**, *2013*, 640428.

72. Turkevich, J.; Stevenson, P. C.; Hillier, J. A Study of the Nucleation and Growth Processes in the Synthesis of Colloidal Gold. *Discuss. Faraday Soc.* **1951**, *11*, 55–75.

73. Morita, M.; Ohmi, T.; Hasegawa, E.; Kawakami, M.; Suma, K. Control Factor of Native Oxide Growth on Silicon in Air or in Ultrapure Water. *Appl. Phys. Lett.* **1989**, *55*, 562–564.

74. Janssen, D.; Palma, R.; Verlaak, S.; Heremans, P.; Dehaen, W. Static Solvent Contact Angle Measurements, Surface Free Energy and Wettability Determination of Various Self-Assembled Monolayers on Silicon Dioxide. *Thin Solid Films* **2006**, *515*, 1433–1438.

75. Torchinsky, I.; Amdursky, N.; Inberg, A.; Rosenman, G. Electron-Induced Adhesion and Patterning of Gold Nanoparticles. *Appl. Phys. Lett.* **2010**, *96*, 093106.

76. Kolíbal, M.; Konečný, M.; Ligmajer, F.; Škoda, D.; Vystavěl, T.; Zlámal, J.; Varga, P.; Šikola, T. Guided Assembly of Gold Colloidal Nanoparticles on Silicon Substrates Prepatterned by Charged Particle Beams. *ACS Nano* **2012**, *6*, 10098–10106.

77. Aronov, D.; Molotskii, M. Wettability Inversion Induced by Weak Electron Irradiation. *J. Appl. Phys.* **2008**, *104*, 114903.

78. Aronov, D.; Molotskii, M.; Rosenman, G. Electron-Induced Wettability Modification. *Phys. Rev. B* **2007**, *76*, 035437.

79. Aronov, D.; Rosenman, G.; Barkay, Z. Wettability Study of Modified Silicon Dioxide Surface Using Environmental Scanning Electron Microscopy. *J. Appl. Phys.* **2007**, *101*, 084901.

80. Egerton, R. F.; Li, P.; Malac, M. Radiation Damage in the TEM and SEM. *Micron* **2004**, *35*, 399–409.

81. Royall, C. P.; Thiel, B. L.; Donald, A. M. Radiation Damage of Water in Environmental Scanning Electron Microscopy. *J. Microsc.* **2001**, *204*, 185–195.

82. Rykaczewski, K.; Chinn, J.; Walker, M. L.; Scott, J. H. J.; Chinn, A.; Jones, W. Dynamics of Nanoparticle Self-Assembly into Superhydrophobic Liquid Marbles during Water Condensation. *ACS Nano* **2011**, *5*, 9746–9754.

83. Rykaczewski, K.; Scott, J. H. J. Methodology for Imaging Nano-to-Microscale Water Condensation Dynamics on Complex Nanostructures. *ACS Nano* **2011**, *5*, 5962–5968.

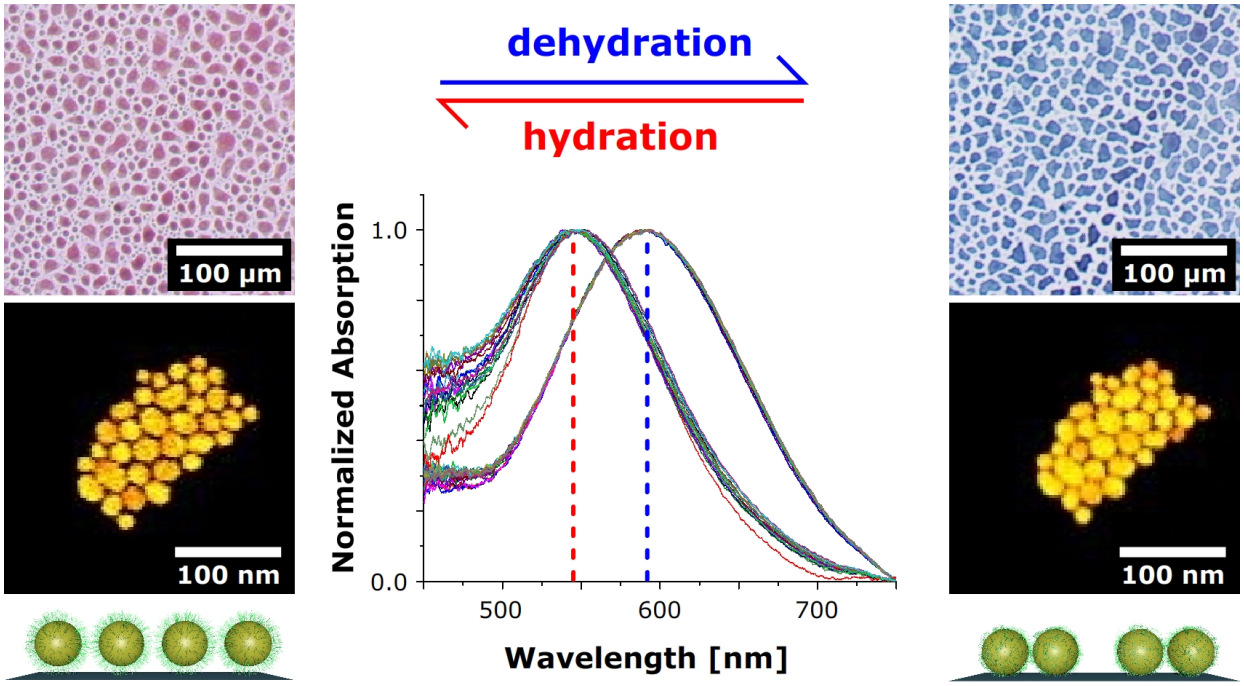
dehydration
hydration
100 µm
100 nm
100 µm
100 nm
Normalized Absorption
1.0
0.0
500
600
700
Wavelength [nm]